Dendritic Growth Morphologies in Al-Zn Alloys—Part I: X-ray Tomographic Microscopy

JONATHAN FRIEDLI, J.L. FIFE, P. DI NAPOLI, and M. RAPPAZ

Upon solidification, most metallic alloys form dendritic structures that grow along directions corresponding to low index crystal axes, *e.g.*, ⟨100⟩ directions in fcc aluminum. However, recent findings[1,2] have shown that an increase in the zinc content in Al-Zn alloys continuously changes the dendrite growth direction from ⟨100⟩ to ⟨110⟩ in {100} planes. At intermediate compositions, between 25 wt pct and 55 wt pct Zn, ⟨320⟩ dendrites and textured seaweeds were reported. The reason for this dendrite orientation transition is that this system exhibits a large solubility of zinc, a hexagonal metal, in the primary fcc aluminum phase, thus modifying its weak solid–liquid interfacial energy anisotropy. Owing to the complexity of the phenomenology, there is still no satisfactory theory that predicts all the observed microstructures. The current study is thus aimed at better understanding the formation of these structures. This is provided by the access to their 3D morphologies *via* synchrotron-based X-ray tomographic microscopy of quenched Bridgman solidified specimens in combination with the determination of the crystal orientation of the dendrites by electron-backscattered diffraction. Most interestingly, all alloys with intermediate compositions were shown to grow as seaweeds, constrained to grow mostly in a (001) symmetry plane, by an alternating growth direction mechanism. Thus, these structures are far from random and are considered less hierarchically ordered than common dendrites.

DOI: 10.1007/s11661-013-1912-7

I. INTRODUCTION

ALUMINUM has a weak anisotropy of the solid–liquid interfacial energy $\gamma_{s\ell}$ (about 1 pct)[3] that can easily be perturbed by the addition of an alloying element with a different crystal structure, such as zinc, a hexagonal element, that exhibits the anisotropy of about 30 pct between the c-axis and the basal plane. It was found by Henry*et al.*[4] and Sémoroz *et al.*[5] that dendrites in Al-Zn could grow along directions different from the usual ⟨100⟩ axes of cubic metals, and more recently, a systematic effect of this alloying element has been identified by Gonzales *et al.*[1,2,6] These authors showed that an increase in the zinc content in Al-Zn alloys continuously changes the dendrite growth direction from ⟨100⟩ to ⟨110⟩ in a {100} plane (Figure 1). At intermediate compositions, *i.e.*, between 25 and 55 wt pct, Gonzales *et al.* observed seaweed-type morphologies at the beginning and end of this dendrite orientation transition (DOT) (areas shaded in gray in Figure 1) and ⟨320⟩ dendrites around 50 wt pct Zn. The seaweed microstructures did not exhibit clear trunks and arms but were nevertheless textured.

JONATHAN FRIEDLI, formerly PhD Student with the Laboratoire de Simulation des Matériaux, Ecole Polytechnique Fédérale de Lausanne, EPFL-STI-IMX-LSMX, Station 12, 1015 Lausanne, Switzerland, is now Development Engineer with NOVELIS Inc., Sierre, Switzerland. J.L. FIFE, Postdoctoral Researcher, is with the Swiss Light Source, Paul Scherrer Institut, 5232 Villigen, Switzerland. P. DI NAPOLI, Postdoctoral Researcher, and M. RAPPAZ, Professor, are with the Laboratoire de Simulation des Matériaux, Ecole Polytechnique Fédérale de Lausanne. Contact e-mail: paolo.dinapoli@epfl.ch
Manuscript submitted March 27, 2013.
Article published online August 20, 2013

This continuous DOT has a direct influence on the texture of directionally solidified alloys,[2] and thus has important implications for controlling the mechanical properties of cast alloys. Since these solidification experiments were conducted at low-to-moderate growth rates, the contribution of attachment kinetics could be discarded as a cause, and these variations of growth morphologies/directions were thus attributed to the influence of zinc on the anisotropy of the solid–liquid interfacial energy $\gamma_{s\ell}$ of the fcc (Al) phase.

In the literature, the seaweed morphology has been predicted theoretically[7] and modeled in 2D[8,9] when the interfacial energy anisotropy is low or nil. It was observed experimentally in constrained 2D growth of transparent organic alloys[10,11] when a crystallographic plane with a degeneracy of the interfacial energy stiffness is parallel to the 2D growth plane.

Observations of seaweed morphologies in 3D growth of metallic alloys are rare. Mullis *et al.*[12] observed them in ultrapure copper and Gonzales *et al.*[1,2,6] in Al-Zn alloys. The major difficulties in the interpretation of the analyzed microstructures, and thus the lack of generalized prediction criteria, arise from the drawbacks of the analysis methods themselves. In fact, the very complex morphologies were, up to now, almost exclusively analyzed in 2D, and their random character was hard to overlook.

There are two examples where these complex 3D morphologies were analyzed in 3D.[13,14] In both studies, optical serial sectioning was used to reconstruct the microstructures. In $Ni_{51}Al_{49}$, solidified at very high velocity (2 m/s), Assadi *et al.* attributed the seaweed

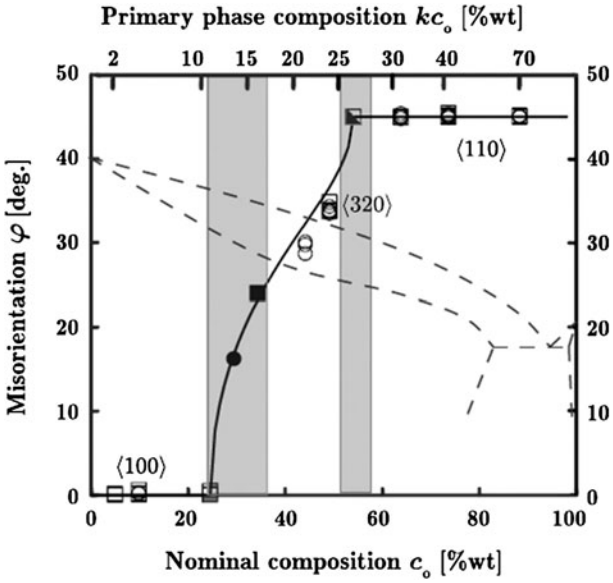

Fig. 1—Angle between the ⟨100⟩ direction and the growth direction of Al-Zn dendrites as a function of the nominal composition, c_0, of Zn (*bottom scale*) and solid composition, kc_0 (*upper scale*), after.[1] The two shaded areas near 25 and 55 wt pct correspond to compositions for which textured seaweed structures were observed (*filled circles* and *squares* indicate in this case the angle between ⟨100⟩ and the preferential direction of the texture). The high-temperature portion of the Al-Zn phase diagram is superimposed in *dashed lines*, with an arbitrary vertical scale.

formation to kinetic effects in this intermetallic alloy. In Al-55 wt pct Zn, Gonzales observed Zn-textured seaweeds. Although this specimen exhibited a ⟨110⟩ texture, its 3D morphology clearly differed from a ⟨110⟩ dendrite exhibiting ⟨110⟩ trunks and arms. The seaweed structure was textured, but was also very tortuous and did not exhibit clear growth directions.

Interestingly, neither of those two studies quenched the growing structure, and thus, diffusion smeared the sharp solid–liquid interface, which made the interpretation of growth directions or more subtle aspects of the microstructure very difficult. Thus, these new microstructures and their 3D growth and orientation selection mechanisms are still poorly understood, and a study with adapted 3D methods is essential to shed light on this phenomenon. The drawbacks of previous analysis methods are

- Metallographic sections, even if prepared in the desired crystallographic orientation, might not be at a desired depth in the sample, for example, at the center of a primary trunk. Thus, even if a trunk seems continuous, coalescence merges secondary arms together, making them indistinguishable from primary trunks.
- Arms are not always attached to the trunk and could falsely be thought to grow in or very close to the prepared section. Especially with high multiplicity dendrites such as ⟨320⟩,[1,5] very small variations in angle make big differences in the interpretation. This and the previous point make any interpretation on secondary arms orientation ambiguous, since they might actually not lie in the considered plane.
- Primary solid is delicate to reveal by etching because of coarsening, backdiffusion, and solid-state transformation (in the present case of Al-Zn, spinodal decomposition). This problem is even more acute at low solute concentration in a system with a large solubility in the primary phase. Solid fraction evolves rapidly near the liquidus, but the temperature remains high and backdiffusion is important, thus smearing the solid–liquid interface.
- A section taken far from the solidification front misses information about the dendrite tip shape and the very beginning of its evolution, where the most dramatic changes in the microstructure occur.

We propose a method enabling the characterization of seaweed and high multiplicity dendritic structures in Al-Zn alloys. The objectives of the current study are to introduce this method, extend the DOT analysis with 3D information about these structures in Al-Zn alloys, and show its applicability to a wide variety of problems. Section II will present the experimental procedure encompassing Bridgman solidification and quenching, metallographic preparation and observation, and X-ray tomographic microscopy, and electron backscattered diffraction (EBSD) measurements. Results for the whole composition range are presented and discussed with a specific focus placed on the Al-50 wt pct Zn alloy in Section III–A. Phase-field simulations of the growth morphologies in Al-Zn alloys are presented in the companion paper.[15]

II. EXPERIMENTS AND METHODS

Nine aluminum-zinc alloys of various compositions ranging from 5 to 90 wt pct Zn were prepared from 99.995 wt pct purity base metals. The alloys were cast in a brass mold ($20 \times 20 \times 250$ mm^3) and then machined into rods 3.6 mm in diameter. The chemical composition of each was verified by EDX. Two aluminum-copper alloys, 4 and 15 wt pct Cu, respectively, were prepared in a similar manner and were used as reference alloys.

A. *Bridgman Solidification and Quenching*

The Bridgman setup is a modified version of the vertical tubular furnace presented by Gonzales and Rappaz[1] in their DOT analysis. The modification consisted of a reduction in diameter of the copper water-cooled tube from 10 to 7 mm^2, allowing for a reduction of the specimen diameter and thus a more efficient quenching. The alloy rods were inserted in quartz or alumina tubes for alloys with liquidus temperatures less than and greater than 913 K (640 °C), respectively. The tubes of 4-mm and 6-mm inner and outer diameters, respectively, and 800-mm length were hung in the furnace by a quick release clamp and pulled

through the furnace at four different velocities (1, 4, 10, and 20 mm/min) in a thermal gradient between 5 and 11 K/mm depending on the alloy properties and the hot-zone temperature. The latter was set to 323 K (50 °C) greater than the liquidus temperature, and the specimen, already partly inserted in the cooler, was left to equilibrate for 30 min before pulling started. After a 100-mm traverse toward the cold zone, the specimen was quickly released (dropped <1 s) into a water quench container, allowing the growing structure to freeze.

Gonzales and Rappaz[1] showed that the pulling velocity, in the range of their Bridgman and directional solidification experiments (*i.e.*, 0.06–3 mm/s), did not influence the DOT. The four velocities in the present case were thus chosen to generate structures fine enough to be representative in the sample volume and coarse enough to be easily distinguishable from the liquid after quenching. The range of cooling rates in the Bridgman furnace varies from 0.08 to 3 K/s, but even if the primary solid is more distinguishable from the quenched liquid at low pulling velocities, the cooling rate during the quench (400 to 600 K/s) leads to a fair contrast even in the most unfavorable set of experimental conditions.

Thermal gradients were characterized in another set of experiments by introducing two *K*-type thermocouples, with a vertical separation of 10 mm, into the melt. The procedure for this set of experiments was exactly the same as for the quench experiments, except that only one sample of each composition (Al-10, 20, 50 and 90 wt pct Zn) was used in this case for all pulling speeds. The samples were totally remelted and allowed to equilibrate for 30 min between each run at different velocities. The acquisition of the temperature data was made through a NetDAQ Data Acquisition System. The absolute precision of the temperature measurement was on the order of 275 K (2 °C).

B. *Metallography*

After solidification, 30-mm-long samples were cut out near the position of the quenched tip, from the ~200-mm-long rod. A longitudinal section of this sample was mirror polished and etched to reveal the structure. The specimen was then imaged over its full length. The obtained micrograph composite, see an example in Figure 2, allowed precise location of the tip of the structure and thus the location of the tomographic microscopy sample to be extracted.

The clear phase separation generated by the quench allows for excellent contrast in both metallographic observations and later in tomographic microscopy, as illustrated in Figure 3 by the comparison between an unquenched and a quenched microstructure. The fact that this method drastically reduces backdiffusion, at least in the region close to the dendrite tip, greatly simplifies both the etching procedures and the interpretation of the observed morphologies.

C. *X-ray Tomographic Microscopy*

In order to access the full 3D structure of the complex growth morphologies, synchrotron-based X-ray tomographic microscopy experiments were performed at the

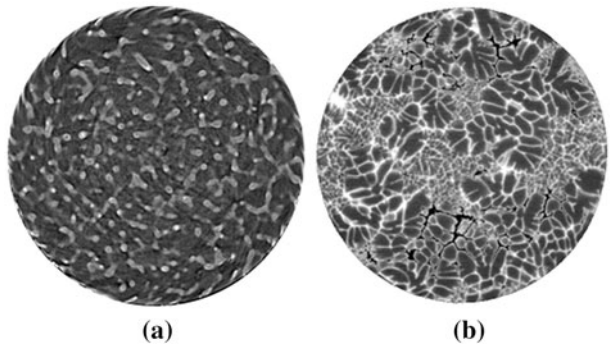

Fig. 3—Cross sections from tomographic microscopy stacks comparing an unquenched (*a*) and quenched (*b*) Al-55 wt pct Zn Bridgman solidified sample, clearly showing the effect of backdiffusion and coarsening. The samples are 700 μm in diameter. The reverse contrast between the different morphological features is given by their chemical composition: the lighter the phase, the richer in heavy elements, in this case zinc. In the quenched specimen (b), the primary solid phase is *dark gray*, the thin zinc-rich segregation layer around it is *white*, the solidification pores are *black*, and the quenched liquid is in *light gray*, actually a mixture of *white* and *dark gray*, making all the features clearly distinguishable. The clockwise spiral-shaped corona at the very edge of (a) originates from the deformation induced during machining of the column. This phenomenon was suppressed by more careful handling of the specimens.

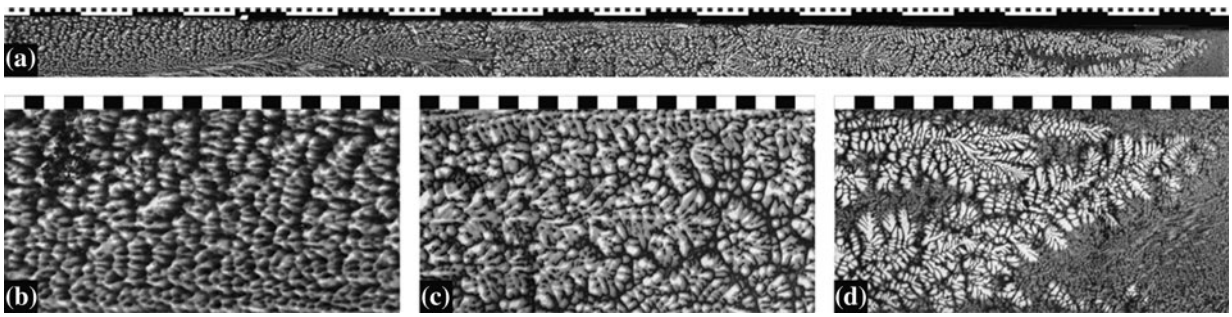

Fig. 2—Metallography of longitudinal sections of a quenched Al-50 wt pct Zn Bridgman sample solidified at 4 mm/min. *Top* 25-mm-long section shows the evolution of the structure away from the tip. Thermal gradient is from *left* to *right*. Small and big divisions of the *top scale* represent 100 μm and 1 mm, respectively. *Bottom* enlargement of three regions of the sample showing the effect of back diffusion and the smearing of the solid–liquid interface. The primary solid phase is *white* and the quenched liquid *dark gray*. The evolution of backdiffusion is clearly visible in the two images on the *left*. The scale divisions represent 100 μm.

TOMCAT beamline of the Swiss Light Source (Paul Scherrer Institute, Villigen, Switzerland).[16] Since the analysis volume accessible through this technique is smaller than the Bridgman sample dimensions, each specimen had to be machined down to the appropriate size at the precise location of the tip of the quenched growth morphology. Two main considerations were taken into account in the selection of the sample diameter. First, for the specimen to be representative, its diameter should contain at least a few characteristic, primary trunk dendrite spacings. Furthermore, for the fine morphological details to be resolved, the pixel size should be smaller than the secondary dendrite arm spacing. It should be recalled that the resolution is at least twice the pixel size, since two pixels are necessary to define an edge and three pixels are necessary to determine a feature. These two factors dictated the choice of the Bridgman solidification conditions. The maximum sample diameter and the achievable pixel sizes were imposed by the field of view of the beamline optics, the X-ray beam energy and the camera resolution, respectively.

Second, aluminum and zinc are very different X-ray absorbers, and thus very different conditions were chosen to accommodate high- *vs* low-alloyed specimens. The X-ray penetration is dependent on the energy, the composition, and thickness of the sample.

The quality of the resulting tomograms is dependent on the signal-to-noise ratio in the image, and we determined that in our case, a minimum of 20 pct X-ray transmission was necessary for high-quality images. For example, to accommodate the highest Zn fraction, Al-90wt pctZn, at 40keV, a sample diameter of 700 μm was chosen.

The acquired data were processed with a filtered backprojection algorithm which generated a stack of transverse cuts for each scan.[17,18] Multiple scans of the height of the sample were taken, aligned, and then merged into one stack to allow for better visualization of the scanned volume.

D. *EBSD*

The reconstructed tomographic microscopy data stacks were searched for widely developed secondary arms near a quenched dendrite tip. A transverse cut was then realized with a diamond blade saw at the same precise location in the column [*e.g.*, dashed line on Figure 4(b)]. The sections were then prepared for EBSD with a mechanical polishing using increasingly fine SiC papers (down to 4000 grade) followed by 1 and 0.25 μm diamond particle sprays. A subsequent electropolishing with an A2 solution (72 mL ethanol, 20 mL 2-buthoxyethanol, and 8 mL perchloric acid at 71 pct concentration) for the duration ranging

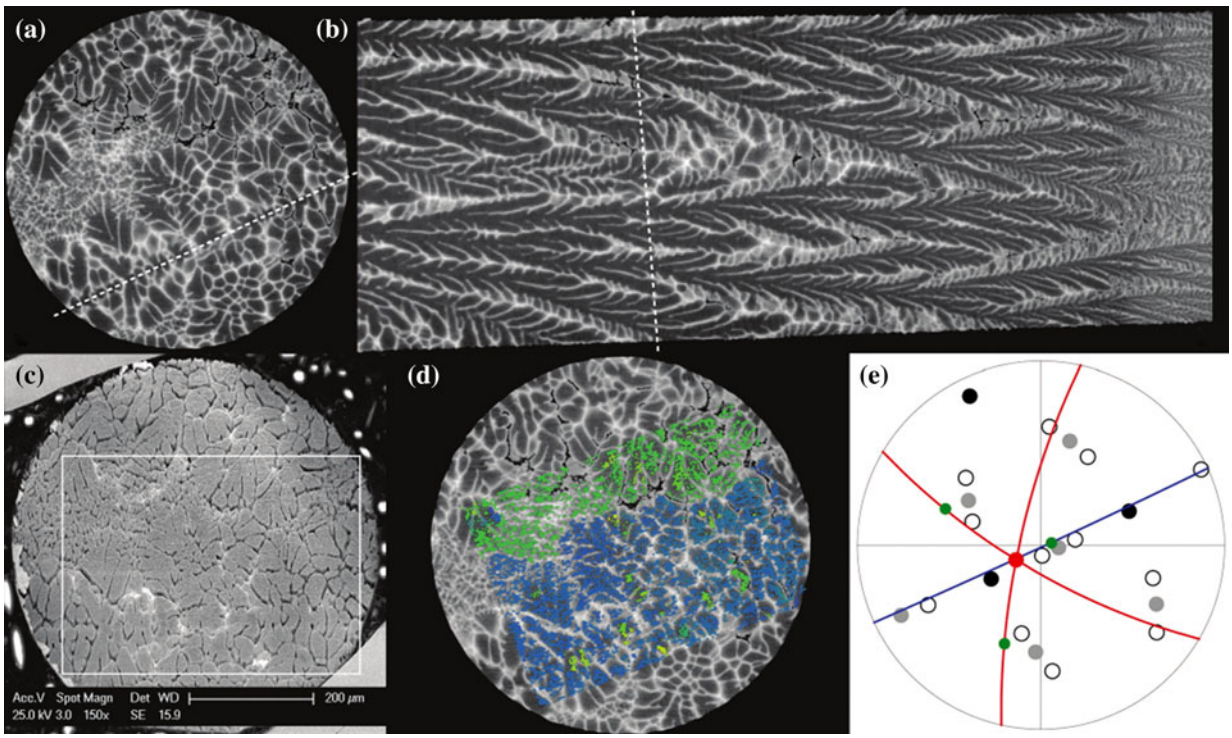

Fig. 4—Transverse (*a*) and longitudinal sections (*b*) of a tomogram of a quenched Al-50 wt pct Zn sample solidified at 4 mm/min. In the longitudinal section, the thermal gradient is from *left* to *right*, and the quenched interface can be seen on the right of the image. The *dashed lines* depict the location of the respective longitudinal and transverse sections. (*c*) SEM micrograph of the cut corresponding to the tomographic section of (a), the white rectangle indicates the location of the EBSD map. (*d*) Same section as (a) with the superimposed EBSD orientation map showing two grains, in *green* and *blue*. (*e*) Typical pole figure of the transverse section in the tomographic microscopy stack coordinate system. The *blue* and red lines correspond to planes of interest. The red and green dots represent the directions of primary trunks and secondary arms, respectively, measured in the 3D reconstruction. The crystallographic orientations obtained from the EBSD map for the corresponding grain (the blue grain in (d)) are shown by black ⟨100⟩, gray ⟨110⟩ and open ⟨320⟩ circles.

from 4 to 10 s at 4 V and 2 s at 25 V removed the deformed surface layer and led to a good indexing ratio of the pseudo-Kikuchi lines.

The EBSD measurements were performed using a XL30-FEG SEM microscope (Philips Electronics Instruments Corp., Mahwah, NJ, USA) equipped with a Nordlys camera (HKL Technology A/S, Hobro, Denmark). The HKL Channel 5 software (HKL Technology A/S) was used for data acquisition and treatment. The following parameters were used for the acquisition of orientation maps of the aluminum primary phase: acceleration voltage ranging from 20 to 25 kV, spot size 4 nm, working distance from 13 to 17 μm, and map step size from 2 to 4 μm. For every map, a reference (001) silicon wafer was used to calibrate the setup. The precision of the system was estimated to be ± 2 deg on the orientation measurement. Stereographic projections are used, and pole figures refer to the upper hemisphere.

The SEM micrograph on which the EBSD orientation map is based [*e.g.*, Figure 4(c)] was used to retrieve the best corresponding plane in the tomography dataset, considering that after tomography, the specimen had to be cut and polished for SEM observations. As Figure 4(b) shows very clearly, it is not always exactly perpendicular to the axis of the sample, but this deviation can be accounted for. The orientation map itself was then superimposed on the tomographic microscopy cut [Figure 4(d)], the grains identified, and their orientation determined. To ensure the best possible alignment, the maps were, when possible, spanned over the whole sample. Knowing the misorientation between the EBSD coordinate system and the tomographic microscopy dataset, the orientation of the grains can be rotated form the former to the latter. All planes and directions identified in the tomographic microscopy stack could then be associated with a crystallographic orientation [*e.g.*, Figure 4(e)].

III. RESULTS AND DISCUSSION

A. *Method Improvements*

As has already been seen in Figures 2 and 3, the proposed method greatly improves the quality and quantity of information that can be extracted from Bridgman-type experiments and enables the clear identification of microstructural features, In particular:

1. Quenching limits the amount of time the sample remains at high temperatures and thus reduces backdiffusion, coalescence, and coarsening near the dendrite tips. This allows microstructural components such as grains, trunks, and arms to be unambiguously determined.
2. The morphology of the dendrite or seaweed tip is clear.
3. The contrast between phases is sufficient even if the liquid and solid compositions are very close, *i.e.*, at low solute compositions [see Figures 5(a, b)].

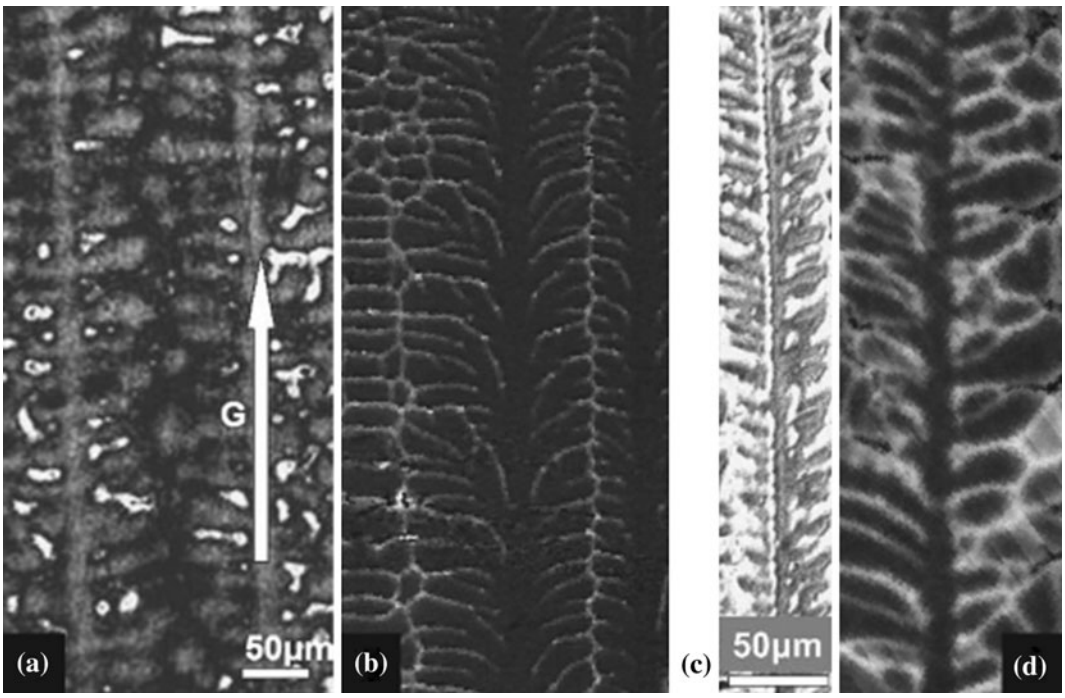

Fig. 5—Bridgman-solidified Al-10 wt pct Zn (*a*, *b*) and Al-50 wt pct Zn (*c*, *d*) samples. (a) Metallographic section in a (100) plane with secondary arms seen at 363 K (90 °C) from the trunk.[1] (b) (100) section cutting a trunk in an X-ray tomographic microscopy dataset from a quenched sample exhibiting a much more precise view of the secondary arms. (c) Reported ⟨320⟩ dendrites[1] showing a trunk with very irregular secondary arms. (d) Cut on the X-ray tomographic microscopy stack with an orientation identical to (c) through a trunk in a (001) plane showing arms that actually grow out of plane. Note that the magnification is identical for (a) and (b), and for (c) and (d), but it does not exactly match between (a, b) and (c, d).

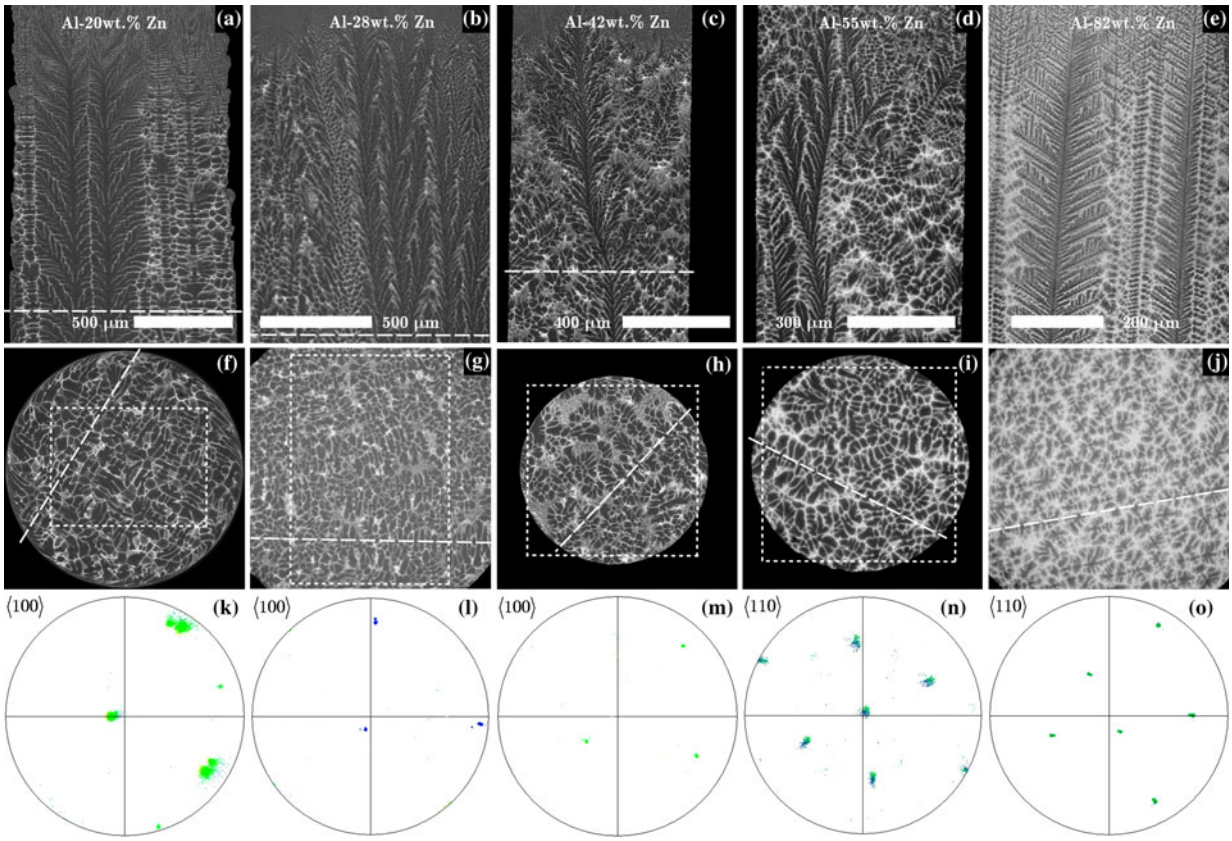

Fig. 6—Longitudinal (*top row*) and transverse (*center row*) cuts through the X-ray tomography stack (the transverse sections *f*, *g*, *h* correspond to the *dashed lines* of longitudinal sections *a*, *b*, *c*, while for figure *i* and *j* they are relative to the bottom sections of *d* and *e*) and pole figure (*bottom row*) associated with the areas highlighted in the transverse cuts. Pole figure *o* is relative to the whole transverse section *j*. From *left* to *right* Al-20 wt pct Zn, Al-28 wt pct Zn, Al-42 wt pct Zn, Al-55 wt pct Zn solidified at 10 mm/min and Al-82 wt pct Zn solidified at 20 mm/min. The trace of the longitudinal section is shown by a *dashed white line* on the transverse cut. Note that whereas the length scale is the same for longitudinal and transverse sections of each alloy, the magnification varies from one alloy to another. In these experiments, a range of objectives (4×, 10×, and 20×) were used; thus, pixel sizes varied from 0.37 to 1.85 μm. EBSD pole figures show a texture matching the results by Gonzales and Rappaz.[1]

4. Because the complete 3D morphology is accessible, the selection of observation planes and the identification of morphological features in such planes are precise and clear.

Two examples of the interpretation improvement provided by this method are shown in Figure 5. In dilute Al-10 wt pct Zn, the secondary arms were believed to grow at an angle of 90 deg with respect to the trunk (Figure 5(a)[1]). However, Figure 5(b) reveals that when cutting exactly through the trunk, secondary arms grow at a smaller angle with respect to the trunk. In the case of the high multiplicity ⟨320⟩ dendrite morphologies reported by Gonzales and Rappaz[1] [Figure 5(c)], the comparison with the tomographic microscopy data of Figure 5(d) shows that the irregularity in the secondary arms comes from out-of-plane growth suggesting an even more complex growth mechanism than previously expected. These salient features allow for the reexamination of the DOT in Al-Zn.

B. *Microstructure Analysis*

X-ray tomographic microscopy was performed on Al-Zn alloys from 5 to 90 wt pct Zn and Figure 6 shows longitudinal and transverse sections through the stack of samples of various compositions. As the sizes of the tomographic microscopy samples and microstructures vary from case to case because of X-ray absorption variations, the magnifications are not exactly the same across the samples. Instead, they were selected to be representative of the typical microstructure observed for each composition.

First, EBSD measurements show an identical angular dependence of the dendrite behavior or seaweed texture as in the DOT for the whole range of Al-Zn alloys, and thereby confirm the results already obtained by Gonzales and Rappaz.[1,2] However, as foretold in the previous section, the secondary dendrite arms in low-alloyed Al and the trunk and arm directions in the intermediate composition range where seaweeds are observed cannot be deduced from the DOT overall misorientation curve of Gonzales and Rappaz (Figure 1).

1. *Symmetries*

The tomographic microscopy data were scouted for specific symmetry planes, appearing in the transverse cuts (Figure 6 center row). Three types of symmetries have been observed in Al-Zn alloys. Between 5 and 20

wt pct Zn, trunks with ⟨100⟩ orientation and secondary arms growing in {100} planes are observed. In transverse sections, those typically appear as crosses with a 90 deg angle (Al-20 wt pct Zn in Figure 6, left center row). At zinc concentrations higher than 55 wt pct, dendrites (both trunks and arms) grow along well-defined ⟨100⟩ directions.

Indeed, in the former studies,[1,14] the transformation at the eutectic temperature [654 K (381 °C)] provided some sort of a self-quench, making the structure to clearly appear (*e.g.*, in Al-82 wt pct Zn Figure 6, right center row). This cut also shows that the growth advantage, and thus the larger lateral extension, ⟨110⟩ arms at 60 deg from the trunk have over the shorter ⟨110⟩ arms that grow at 90 deg In the range from 25 to 55 wt pct Zn, those symmetries break down and an apparently random structure is observed. Nonetheless, a careful look through the X-ray tomographic microscopy stacks allows one to identify individual symmetry planes in each grain, such as the ones delineated in Figure 6 center row for Al-28, 42 and 55 wt pct Zn.

The EBSD pole figures show that in all intermediate compositions investigated, this symmetry plane is a (100) plane, as shown in more detail in the example of Al-50 wt pct Zn [Figure 4, blue line in the pole figure (e) parallel to the white dashed line in the corresponding cross section (a)]. This finding is in agreement with the previous studies by Gonzales *et al.* since the DOT operates in a (100) plane.

2. *Primary trunk orientation*

Low- and high-alloyed Al-Zn alloys exhibit primary dendrite trunks which clearly grow in well-defined ⟨100⟩ and ⟨110⟩ directions, respectively. At intermediate compositions, the situation is more complex since none of these alloys produce a typical dendritic structure, and thus no trunk in the classical sense is present. The top row of Figure 6 shows longitudinal cuts in the symmetry (100) plane of three such alloys, which all exhibit a seaweed-type behavior. Instead of well-established trunks, the growth seems to occur in an alternating tip splitting mechanism with very short arms. The structure is not random, however, since certain orientations seem to be preferred in the alternating splitting process. Even if the morphology differs significantly from that of a typical dendrite, one can still identify certain features using the names of more commonly observed structures. We will call a feature a "trunk" if it is aligned within about 20 deg to the thermal gradient, and extends over a distance large enough to be clearly identifiable by a number of side branches. Although this definition is imprecise, the trunks in Figure 6 are nevertheless clear. Any smaller feature which emerges from such a trunk will be called an arm.

To make a meaningful assertion about the trunks, a minimum number of them showing similar characteristics should be present in a cut. Thus, the sample showing (100) symmetry plane with the largest number of trunks [Al-50 wt pct Zn, Figure 4(b)] was selected and examined in more detail.

As shown by the solid and dashed white lines in Figure 7(a), two types of trunks were observed. Those oriented close to vertical (dashed lines, *e.g.*, B), *i.e.*, the thermal gradient direction, show secondary arms on both sides in the (100) plane, whereas those further inclined (solid lines, *e.g.*, A1) exhibit arms on only one side in the plane.

Note that since the secondary arms are so short and rarely straight, their direction, even taken as the average of the angle with the trunk found at the root, is subject to large errors. However, the different characteristics observed for type A and B trunks remain valid. Figure 7(e) shows that the latter grow within a few degrees from the ⟨320⟩ direction whilst the former are

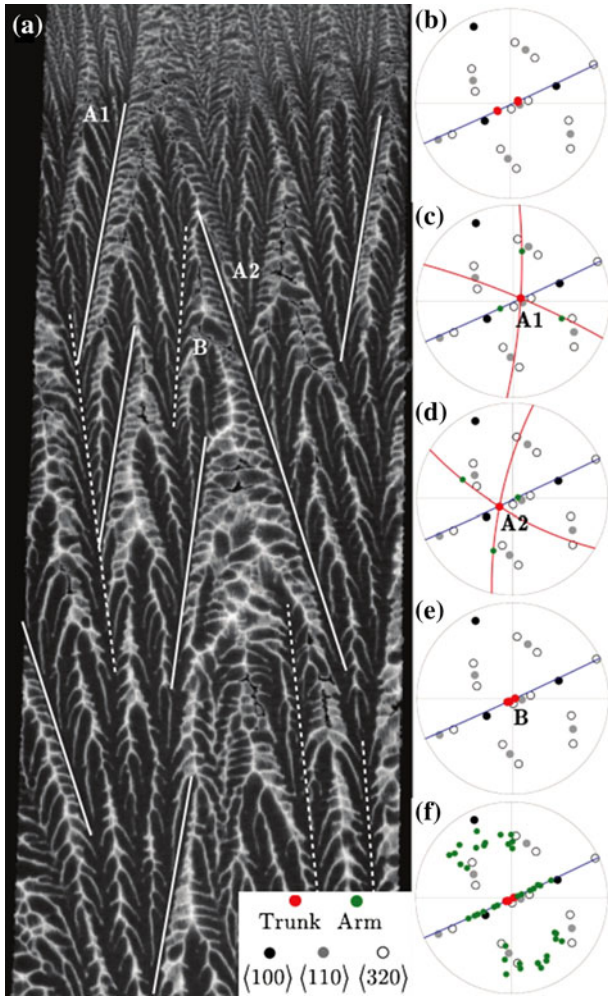

Fig. 7—(*a*) (100) symmetry plane in Al-50 wt pct Zn, showing two types of trunks. Trunks with secondary arms on only one side in the (100) plane, highlighted by *solid white lines*, and trunks with arms on both sides identified by *dashed white lines*. (*b–f*) are the pole figures obtained from the EBSD map in Figure 4(d) with the ⟨320⟩ direction being the closest to the vertical, *i.e.*, the thermal gradient direction. The planes and directions found in the X-ray tomography stack are superimposed on the pole figures. The (100) symmetry plane is represented in blue. Red and green dots represent trunks and arms, respectively. (b) shows the orientation of the A-type trunks. The configuration of the trunk, secondary arms and (*red*) planes in which the latter lay are shown in (c) and (d) for trunk A1 and A2, respectively. (e) shows the orientation of the B-type trunks, close to the ⟨320⟩ direction. (f) shows the directions of the secondary arms associated with the B-type trunks.

much more regularly oriented in two directions at ~14 deg with respect to ⟨320⟩ (Figure 7b).

After having examined out of this plane, the secondary arms emerging from type A trunks are found in two other planes outlined by the two red plane traces in the corresponding stereographic projections. Figure 7(c) and d illustrate this configuration for the trunks A1 and A2. The orientation of these arms in the out-of-plane sections is so ill-defined that it is not possible to identify them with a crystallographic direction with any precision. The in-plane secondary arms orientation on the other hand, corresponds to the direction of the trunks lying on the other side of the ⟨320⟩ direction, *i.e.*, the in-plane arms of trunk A1 are in the same direction as the trunk A2 and vice-versa. This probably explains why over long distances, a zigzag of the trunks is observed. As such, a trunk encounters a perturbation (*e.g.*, the solute field from another trunk or thermal fluctuations), it might switch sides and take the alternate direction. Another example of this phenomenon is shown for Al-42 wt pct Zn in the top row of Figure 6.

The observation of B-type trunks reveals a very different configuration. The scatter of the directions in Figure 7(f) shows that the secondary arms do not seem to have a preferred growth direction. The potential growth disadvantage that result could very well explain their shorter lateral extension compared with the type A configuration.

As the segmentation of such complex and intricate structures cannot be automated, the isolation of one single trunk is hardly accessible and impedes a deeper stereological analysis. Furthermore, this is a static postmortem observation of a highly dynamic process, and *in situ* investigations could certainly improve the understanding of this growth morphology.

The observations in Al-50 wt pct Zn show that the measurement of the texture of such a sample can be deceptive. Indeed, although the mean growth direction, *i.e.*, the texture is ⟨320⟩, by far not all actual growth directions correspond to this orientation as evidenced by A-type trunks.

3. *Secondary arm bending*

Low zinc content alloys, as well as seaweeds, showed that secondary arms have a tendency to bend *away* from the trunk during growth. This observation is counterintuitive because, in most alloys, such as succinonitrile (SCN)–acetone,[19] the arms tend to turn toward the thermal gradient as they grow away from the trunk or, in the case of Ni-based superalloys for which the anisotropy is large, they remain orthogonal to the trunks.[20]

One possible explanation for this growth is that the anisotropy and composition being strongly linked, as seen for the trunks, the arms would bend as a result of the compositional increase in the depth of the mushy zone. Thus, the change of composition of the solid continuously forming on the arm modifies the anisotropy of $\gamma_{s\ell}$ and the growth direction accordingly. This could explain the evolving preferred growth direction observed. It should be noted that in some Al alloys solidified under high thermal gradient, even the primary trunks were observed to bend by Henry *et al.*,[4] which could be another manifestation of the same phenomenon. However, given the DOT of the trunks, this explanation does not stand since the phenomenon should be the opposite of what is observed (Al-20 wt pct Zn in Figure 6) for low solute Al-Zn alloys, with arms bending from ⟨100⟩ at low zinc content to ⟨110⟩ when the zinc content increases.

From an experimental point of view, this phenomenon is hard to quantify precisely in low-alloyed Al-Zn, because the solid fraction evolves rapidly with temperature, leading to short secondary arms, the growth direction of which is difficult to determine. Moreover, secondary arms not only bend, but also have a tendency to split, appearing like a palm-tree, a behavior which is typical for the seaweeds encountered at intermediate compositions.

For the purpose of comparison, Al-Cu alloys were also analyzed [Figures 8(c) and (d)]. Astonishingly, even when the weak anisotropy of aluminum is reinforced by another fcc element, the secondary dendrite arms of Al-4 wt pct Cu show the same type of behavior as in low solute content Al-Zn alloys. The arms have angles with respect to the trunk between 45 and 70 deg at their root, then bend and split further away from the trunk. In a 15 wt pct Cu content alloy, secondary arms grow perpendicular to the trunk, as would be expected for a cubic solute element such as copper which reinforces the weak anisotropy of Al. However, at the very root of the arms, the take-off angle is still slightly smaller than 90 deg. Thus, even though the situation is clearer since the higher copper content* gives more time for the secondary arms to grow, there is still no model that satisfactorily explains these observations.

*in a system with also a smaller partition coefficient and a higher liquidus slope compared with Al-Zn

It appears that aluminum has an inherent character to form ⟨100⟩ trunks with off-crystallographic axis secondary arms, and only a sufficient addition of solute element allows them to stabilize them in a given direction, ⟨100⟩ for copper and ⟨110⟩ for zinc, the latter with an associate change of the primary trunk direction.

Finally, another possible explanation for these observations could be that at low anisotropy, secondary arms start to emerge close to the dendrite tip. For example, in low anisotropy SCN, secondary arms emerge about $2R_{tip}$ behind the tip, whereas that distance is approximately $7R_{tip}$ in pivalic acid which has the anisotropy one order of magnitude higher than SCN.[21] At low anisotropy, the arms thus emerge where the iso-concentration lines form a large angle with respect to the primary trunk direction. Since growth is the fastest along the highest solute gradient, arms might thus start to grow perpendicular to the iso-concentrations and continue to do so as long as the contribution from this gradient is dominant. Further away from the tip and deeper in the mushy zone, the anisotropy contribution takes over and the arms bend. The interdendritic liquid

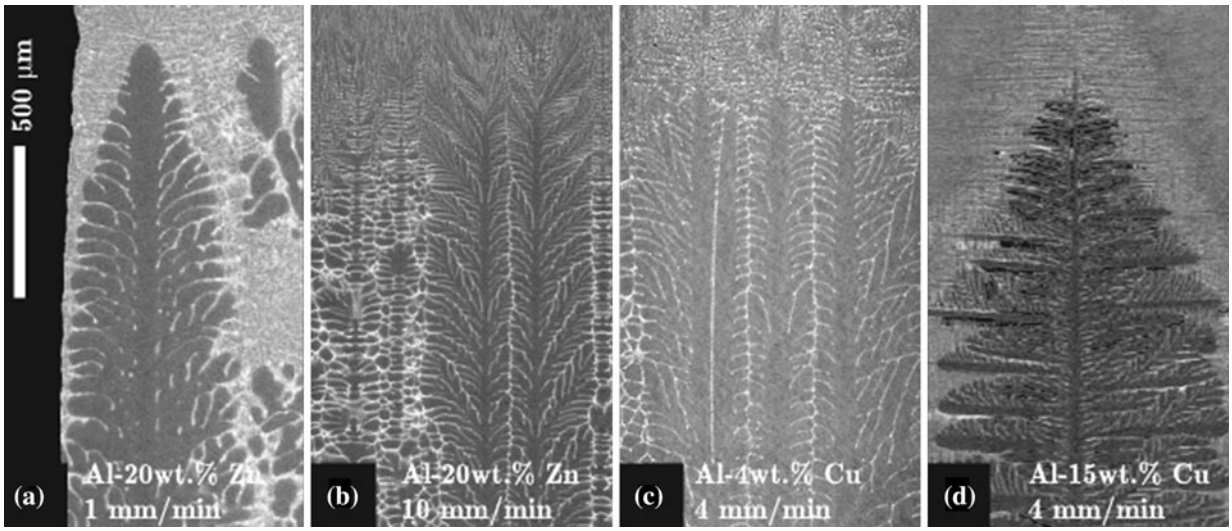

Fig. 8—Tomography sections [(100) plane] through dendrite trunks of 4 specimens.

surrounding the secondary arms in an Al-20 wt pct Zn alloy reaches the composition range where seaweed structures are observed for primary growth, and indeed one observes alternating growth directions of the secondary arms in this alloy. For Al-4 wt pct Cu, anisotropy might still be too weak to constrain the growth of the arms, as it is probably the case for Al-5 and 10 wt pct Zn, whereas in Al-15 wt pct Cu, the arms start perpendicular to the iso-concentration contours, but later follow the ⟨100⟩ direction imposed by the higher anisotropy because of their richer copper composition. This would also explain why nickel secondary arms grow only orthogonal to the trunks first, they emerge later because of the strong anisotropy sharpening and stabilizing the tip. Thus,, when they emerge, the solute concentration gradient is already almost perpendicular to the trunk. One should also note that in these alloys, anisotropy furthermore constrains the arms along ⟨100⟩.

IV. CONCLUSIONS

A method to investigate growth morphologies in metallic systems, featuring X-ray tomographic microscopy of quenched Bridgman samples was presented. Focusing on the analysis of complex microstructures in Al-Zn alloys, the advantages of this method over other techniques were shown by the clear identification of microstructural features that were not observable before.

The investigations of the whole hypoeutectic range of Al-Zn alloys, first confirmed the DOT and the texture observations made by Gonzales and Rappaz.[1] At zinc concentrations higher than 55 wt pct Zn, dendrites grow in well-defined ⟨100⟩ directions. Below 25 wt pct Zn, primary trunks grow along ⟨100⟩, but the secondary arms do not follow these directions and show an unexpected palm-tree behavior.

Seaweed structures were identified at all compositions between 25 and 55 wt pct Zn and could for the first time be characterized in 3D in a metallic alloy with unprecedented details about texture, growth directions, and mechanisms. It was shown that seaweeds are far from random, and the growth was confirmed to be constrained within a symmetry (100) plane. However, new findings showed that the observed macroscopic texture which follows the DOT curve of Gonzales and Rappaz[1] does not necessarily correspond to the actual growth directions of the morphology. The growth seems to operate by an alternating growth direction mechanism and could be linked to the competition between ⟨100⟩ and ⟨110⟩ characters, which was observed in equiaxed growth.[6,15,22]

Although progress was made in the understanding of the microstructure formation mechanisms in Al-Zn alloys, some open questions remain. X-ray tomographic microscopy continues to be a critical tool for examining solidification microstructures, especially as high spatial resolutions are achievable with high temporal resolutions; thus, time-resolved, *in situ* solidification is a reality and can be used to broaden the spectrum of information available for interpretation. For example, the study of seaweed or palm-tree secondary arm growth would certainly most benefit from this technological progress. Further, the recently developed laser-based heating system at the TOMCAT beamline enables the *in situ* observation of growth phenomena in metallic systems in both near-isothermal and directional temperature gradients.[23]

ACKNOWLEDGMENTS

The authors gratefully acknowledge the financial support of the Fonds National Suisse pour la recherche scientifique (Grant No 200020-113260 and 121598), of the Swiss Competence Centre for Materials Science and Technology (CCMX), as well as the financial and technical support from the Paul Scherrer

Institute. They would also like to thank Sam MacDonald and André Phillion for their previous assistance during the X-ray tomographic microscopy sessions at the Swiss Light Source. All electron microscopy measurements were obtained at the Centre Interdisciplinaire de Microscopie Electronique (CIME) of the Ecole Polytechnique Fédérale de Lausanne (EPFL).

REFERENCES

1. F. Gonzales and M. Rappaz: *Metall. Mater. Trans. A*, 2006, vol. 37A, pp. 2797–2806.
2. F. Gonzales and M. Rappaz: *Metall. Mater. Trans. A*, 2008, vol. 39A, pp. 2148–60.
3. S. Liu, R.E. Napolitano, and R. Trivedi: *Acta. Mater.*, 2001, vol. 49 (20), pp. 4271–76.
4. S. Henry, T. Minghetti, and M. Rappaz: *Acta. Mater.*, 1998, vol. 46 (18), pp. 6431–43.
5. A. Semoroz, Y. Durandet, and M. Rappaz: *Acta. Mater.*, 2001, vol. 49 (3), pp. 529–41.
6. T. Haxhimali, A. Karma, F. Gonzales, and M. Rappaz: *Nat. Mater.*, 2006, vol. 5 (8), pp. 660–64.
7. E. Brener, H. Müller-Krumbhaar, and D. Temkin: *Phys. Rev. E*, 1996, vol. 54 (3), pp. 2714–22.
8. E. Brener, T. Ihle, H. Müller-Krumbhaar, Y. Saito, and K. Shiraishi: *Physica A*, 1994, vol. 204, pp. 96–110.
9. H. Emmerich, D. Schleussner, T. Ihle, and K. Kassner: *J. Phys.*, 1999, vol. 11 (46), pp. 8981–93.
10. S. Akamatsu, G. Faivre, and T. Ihle: *Phys. Rev. E*, 1995, vol. 51 (5), pp. 4751–80.
11. S. Akamatsu and G. Faivre: *Phys. Rev. E*, 1998, vol. 58 (3), pp. 3302–15.
12. A.M. Mullis, K.I. Dragnevski, and R.F. Cochrane: *Mater. Sci. Eng. A.*, 2004, vols. 375–377 (1-2 SPEC. ISS.), pp. 157–62.
13. H. Assadi, M. Oghabi, and D.M. Herlach: *Acta. Mater.*, 2009, vol. 57 (5), pp. 1639–47.
14. F. Gonzales. Ph.D. Thesis, Ecole Polytechnique Fédérale de Lausanne (2009).
15. J.A. Dantzig, P. Di Napoli, J. Friedli, and M. Rappaz: *Metall. Mater. Trans. A*, 2013. DOI: 10.1007/s11661-013-1911-8.
16. M. Stampanoni, A. Groso, A. Isenegger, G. Mikuljan, Q. Chen, A. Bertrand, S. Henein, R. Betemps, U. Frommherz, P. Böhler, D. Meister, M. Lange, and R. Abela: in *Proc SPIE 6318* U. Bonse, ed., 2006, 63180M.
17. C. Hintermüller, F. Marone, A. Isenegger, and M. Stampanoni: *J. Synchrotron. Radiat.*, 2010, vol. 17 (4), pp. 550–59.
18. F. Marone and M. Stampanoni: *J. Synchrotron. Radiat.*, 2012, vol. 19, pp. 1029–37.
19. M.E. Glicksman: *Mater. Sci. Eng.*, 1984, vol. 65 (1), pp. 45–55.
20. M. Rappaz and E. Blank: *J. Cryst. Growth*, 1986, vol. 74 (1), pp. 67–76.
21. N.B. Glicksman and ME Singh: *J. Cryst. Growth*, 1989, vol. 98 (3), pp. 277–84.
22. J. Friedli, J. Fife, P. Di Napoli, and M. Rappaz: in *Proc MCWASP* A. Ludwig, ed., 2012.
23. J. Fife, M. Rappaz, M. Pistone, T. Celcer, G. Mikuljan, and M. Stampanoni: *J. Synchrotron. Radiat.*, 2012, vol. 19, pp. 352–58.